NANO · MICRO small
www.small-journal.com

Substitutionally Doped $MoSe_2$ for High-Performance Electronics and Optoelectronics

Fang Zhong, Jiafu Ye, Ting He, Lili Zhang,* Zhen Wang, Qing Li, Bo Han, Peng Wang, Peisong Wu, Yiye Yu, Jiaxiang Guo, Zhenhan Zhang, Meng Peng, Tengfei Xu, Xun Ge, Yang Wang, Hailu Wang, Muhammad Zubair, Xiaohao Zhou, Peng Gao, Zhiyong Fan, and Weida Hu**

2D materials, of which the carrier type and concentration are easily tuned, show tremendous superiority in electronic and optoelectronic applications. However, the achievements are still quite far away from practical applications. Much more effort should be made to further improve their performance. Here, p-type $MoSe_2$ is successfully achieved via substitutional doping of Ta atoms, which is confirmed experimentally and theoretically, and outstanding homojunction photodetectors and inverters are fabricated. $MoSe_2$ p–n homojunction device with a low reverse current (300 pA) exhibits a high rectification ratio (10^4). The analysis of dark current reveals the domination of the Shockley–Read–Hall (SRH) and band-to-band tunneling (BTB) current. The homojunction photodetector exhibits a large open-circuit voltage (0.68 V) and short-circuit currents (1 µA), which is suitable for micro-solar cells. Furthermore, it possesses outstanding responsivity (0.28 A W^{-1}), large external quantum efficiency (42%), and a high signal-to-noise ratio (≈10^7). Benefiting from the continuous energy band of homojunction, the response speed reaches up to 20 µs. Besides, the Ta-doped $MoSe_2$ inverter exhibits a high voltage gain (34) and low power consumption (127 nW). This work lays a foundation for the practical application of 2D material devices.

1. Introduction

2D materials have attracted lots of attention to electronic and optoelectronic devices owing to van der Waals interaction, large carrier mobility, and large absorption coefficients. Among enormous 2D materials, transition metal dichalcogenides (TMDCs) have been deeply explored, due to the moderate bandgap, tunable conductance type, and good stability.[1–3] A variety of functional TMDC electronic and optoelectronic devices are fabricated and reported, such as photodetectors and inverters. Graphene/$MoTe_2$/graphene device and WSe_2/MoS_2 device have been demonstrated with high responsivity.[4–5] MoS_2/WS_2 device and WSe_2/Bi_2Te_3 device show fast response.[6,7] Inverters based on MoS_2/BP or $MoTe_2$ junction have been reported with high gain.[8,9] Despite vast achievements realized, most of them are composed of heterojunctions according to the general conduction types of TMDCs.

F. Zhong, J. Ye, T. He, L. Zhang, Z. Wang, P. Wang, P. Wu, Y. Yu, J. Guo, Z. Zhang, M. Peng, T. Xu, X. Ge, Y. Wang, H. Wang, M. Zubair, X. Zhou, W. Hu
State Key Laboratory of Infrared Physics
Shanghai Institute of Technical Physics
Chinese Academy of Sciences
Shanghai 200083, China
E-mail: heting@ucas.ac.cn; zhanglili@mail.sitp.ac.cn; wdhu@mail.sitp.ac.cn

F. Zhong
School of Physical Science and Technology
ShanghaiTech University
Shanghai 201210, China

F. Zhong, J. Ye, T. He, L. Zhang, Z. Wang, P. Wang, P. Wu, H. Wang, W. Hu
School of Electronic, Electrical and Communication Engineering
University of Chinese Academy of Sciences
Beijing 100049, China

The ORCID identification number(s) for the author(s) of this article can be found under https://doi.org/10.1002/smll.202102855.

T. He, Q. Li, W. Hu
Hangzhou Institute for Advanced Study
University of Chinese Academy of Sciences
Hangzhou 310024, China

B. Han, P. Gao
Electron Microscopy Laboratory and International Center for Quantum Materials
School of Physics
Peking University
Beijing 100871, China

P. Gao
Collaborative Innovation Centre of Quantum Matter
Beijing 100871, China

Z. Fan
Department of Electronic and Computer Engineering
The Hong Kong University of Science and Technology
Hong Kong 999077, China

DOI: 10.1002/smll.202102855

However, heterojunctions based on the general conduction types of TMDCs commonly limit the performance of devices and their further widespread applications. For example, a large band offset of 2D material heterojunction devices severely hinders carrier transport and further leads to poor optoelectronic performance with a low responsivity and slow response speed. In this regard, homojunction devices are desired and considered as a great potential candidate for excellent optoelectronic devices.

Modulation of conduction type is the key technology for homojunction, and many doping methods are developed. A popular and common way is the external field modulation, such as the gate-induced electric field or ferroelectric field.[10,11] The field-induced method flexibly modulates conduction type. However, the applied gate limits the device size and increases the power consumption of electric circuits. Surface functionalization is also used to switch conduction types via chemical treatment.[12] However, the stability of chemical treatment needs further improvement. Above doping methods are more effective for thinner flakes. Compared with the external field modulation and chemical treatment, substitutional doping during the growth process of 2D materials is a more effective and stable method.[13–15] Mo-doped ReS_2 photodiode shows a rectification ratio of 150.[16] The photodetector based on Sb-doped SnS_2 exhibits a response time of less than 8 ms.[17] Ta-doped WSe_2 was synthesized and the corresponding homojunction photodetector was reported with a response speed of 38.9 µs but a low responsivity of 95 mA W^{-1}.[18] Chee et al. realized F-doped MoS_2 and utilized it to fabricate an inverter with the gain of 8.2.[19] Despite the aforementioned achievements, it is still urgent to further improve the performance of electronic and photoelectronic devices for further applications.

Here, we demonstrate excellent homojunction photodetectors and inverters based on the synthesized n-type $MoSe_2$ and p-type $MoSe_2$ via Ta doping. By gradually increasing the percentage of Ta element, the conductance type of the grown $MoSe_2$ crystals changes from n-type to ambipolar, and to p-type, while the crystal structure of $MoSe_2$ remains unchanged. A high-performance homojunction photodetector, consisting of n-type and p-type $MoSe_2$, is achieved. The photodetector operates under zero bias voltage and zero gate voltage, which means that it can serve as a low power consumption device. Thanks to the homojunction, it exhibits a high external quantum efficiency (EQE) of up to 42% and responsivity of 0.28 A W^{-1}. The open-circuit voltage reaches up to 0.68 V. Simultaneously, it operates fast with the rise and fall time of 34 and 20 µs, respectively. Additionally, the inverter based on the synthesized $MoSe_2$ exhibits a high voltage gain of 34. Importantly, its power consumption is merely 126 nW. Our work exhibits the unique advantages of element doping and paves the way toward the practical applications of 2D materials.

2. Results

2.1. Synthesis and Characterizations of Ta-Doped $MoSe_2$

We synthesized undoped and Ta-doped $MoSe_2$ crystals by the chemical vapor transport (CVT) method (more details in the Experimental Section). The optical images of synthesized undoped and Ta-doped $MoSe_2$ are presented in **Figure 1**a and Figure S1 in the Supporting Information, respectively. Both scale sizes of undoped and Ta-doped $MoSe_2$ crystals can be as large as up to three millimeters. The shiny and wrinkle-free surfaces and regular edges are obviously shown, which indicates high-quality $MoSe_2$ crystals. X-ray diffraction (XRD) patterns are performed to further confirm the crystal structure of undoped and doped $MoSe_2$, shown in Figure 1b. Main peaks of undoped $MoSe_2$ are located at ≈13.72°, 27.6°, 41.88°, and

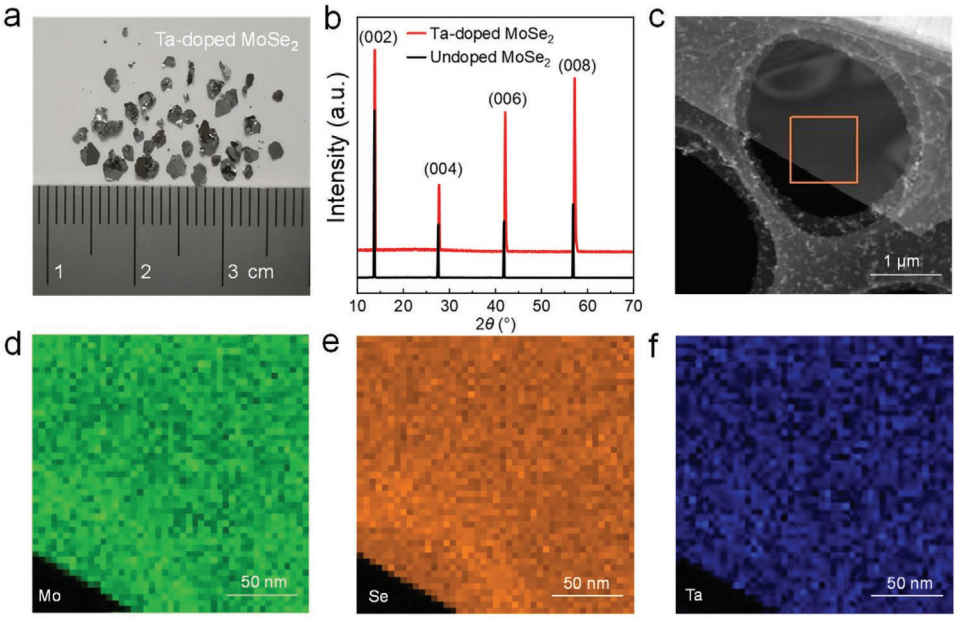

Figure 1. Characterizations of Ta-doped $MoSe_2$ crystals. a) Optical image of synthesized Ta-doped $MoSe_2$ crystals. Scale size of most Ta-doped $MoSe_2$ flakes reaches up to few millimeters. b) XRD pattern of $MoSe_2$ crystal with and without Ta doping. c) Low-magnification STEM image of Ta-doped $MoSe_2$ flake. d–f) Elemental distributions obtained from the orange box in panel (c).

56.88°, which correspond to (002), (004), (006), and (008) crystal orientations, respectively, consistent with the pattern of the standard $MoSe_2$ card (JCPDS-NO.29-0914 in Figure S2a in the Supporting Information). One can find that the pattern of Ta-doped $MoSe_2$ shows similar peaks to that of the standard pattern, which indicates that Ta-elemental doping does not change the intrinsic hexagonal crystal structure of $MoSe_2$. Both the synthesized $MoSe_2$ crystals are grown along the *c*-axis. Additionally, more detailed XRD patterns are shown in Figure S2b in the Supporting Information, and relevant lattice constants (*a* and *c*) are acquired and shown in Note S1 and Table S1 in the Supporting Information. The lattice constant *c* and the ratio *c*/*a* decrease after Ta doping, which indicates substitutional doping, not interstitial doping.[20] Figure 1c shows the low-magnification scanning transmission electron microscopy (STEM) image of the few-layer Ta-doped $MoSe_2$. Furthermore, energy-dispersive X-ray (EDS) spectra are conducted in the orange box to identify the elements of the grown material. Figure 1d–f shows the elemental distributions of Mo, Se, and Ta, respectively. It is obvious that Ta element is successfully doped. The Ta concentration is derived from X-ray photoelectron spectroscopy (XPS) spectra (Figure S3, Supporting Information) and is listed in Table S2 in the Supporting Information. Although the measured concentration is slightly larger than the nominal value (molar ratio of mixed powder for CVT), the Ta concentration in the synthesized $MoSe_2$ can be effectively changed with the molar ratio of the mixture. Except for additional instructions, the later mentioned Ta concentration corresponds to the nominal value for easy comprehension. Additionally, atomically resolved STEM is used to further confirm substitutional doping. **Figure 2**a,d shows the annular dark-field scanning transmission electron microscopy (ADF-STEM) images of undoped and Ta-doped $MoSe_2$ samples, respectively. Mechanically exfoliated $MoSe_2$ samples are prepared and then transferred to a transmission electron microscopy (TEM) grid by the PDMS-assisted method. Contaminants are induced and adhere to the surface of the copper grid, as shown in Figure 2d. However, the results are not affected by the contaminants. Figure 2b shows the atomic-resolution ADF-STEM image, of which the contrast intensity is positively related to atomic number. From ADF-STEM images, each Mo atom is surrounded by three Se atoms. Notably, undoped $MoSe_2$ is a 2H phase, consistent with the previous work.[21,22] For the ADF-STEM image of Ta-doped $MoSe_2$, there are some atomic positions with brighter contrast, which correspond to Ta atoms due to their large atomic number, marked by violet circles in Figure 2e. Combined with the XRD results, the doping method is substitutional doping. For no matter undoped or Ta-doped $MoSe_2$, fast Fourier transform (FFT) of the STEM images are identical and show the six-fold symmetry (Figure S4, Supporting Information). It also demonstrates the hexagonal crystal structure of $MoSe_2$ does not change after Ta doping.

The valence electron of Ta atom is one less than that of Mo atom, thus substitutional Ta atom would serve as the acceptor. The substitutional doping will result in a p-doping in $MoSe_2$. To demonstrate the change of conduction type, both theoretical simulations and experimental characterizations are conducted in our work. Energy band structures are obtained by first-principles calculations based on density functional theory (DFT). Monolayer undoped $MoSe_2$ possesses a direct bandgap of ≈1.5 eV (Figure S5a, Supporting Information). Bulk undoped $MoSe_2$ changes into indirect bandgap semiconductor and the bandgap is ≈1.0 eV (Figure 2c), which is in agreement with previous reports.[23] After the doping, defect states are introduced into both valence and conduction bands. Notably, Fermi level shifts toward to valence band for both monolayer and bulk

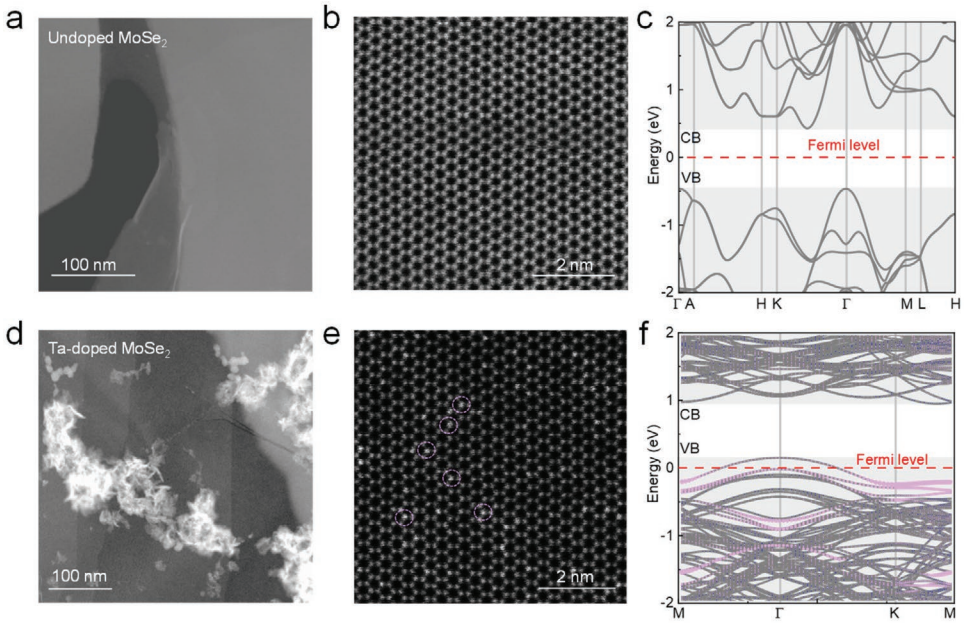

Figure 2. STEM characterization and energy band calculations of undoped $MoSe_2$ and Ta-doped $MoSe_2$. a,b) ADF-STEM images of undoped $MoSe_2$ flake. c) Energy band structure of undoped $MoSe_2$. d,e) ADF-STEM images of Ta-doped $MoSe_2$ flake. Doped Ta atoms are marked by dashed violet circles. f) Energy band structure of Ta-doped $MoSe_2$.

Ta-doped $MoSe_2$, which shows a p-type $MoSe_2$ semiconductor (Figure S5b, Supporting Information; Figure 2f). The p-doping is also demonstrated by Raman spectra. As shown in Figure S6c in the Supporting Information, there are three obvious modes (A_{1g} ≈241 cm^{-1}, E^1_{2g} ≈285 cm^{-1}, and B^1_{2g} ≈353 cm^{-1}), which is consistent with the previous reports.[24,25] Among them, A_{1g} mode is sensitive to both the number of layers and doping concentration.[25] Avoiding the effect of the thickness, undoped and 1% Ta-doped $MoSe_2$ with the same number of layers is used for Raman measurement. The thickness of $MoSe_2$ is identified by atomic force microscopy (AFM) (Figure S6a,b, Supporting Information). The thickness of both undoped and doped $MoSe_2$ is approximately four layers. Figure S6d in the Supporting Information shows magnified Raman spectra. Obviously, the A_{1g} mode is blueshifted for the Ta-doped $MoSe_2$, which confirms the p-doping induced by Ta elements.

Moreover, the conductance type closely depends on the percent of Ta element in $MoSe_2$. Field-effect transistor (FET) devices with various Ta-doped $MoSe_2$ (undoped, 1%, 2%, and 3%) are fabricated on the silicon substrates covered with 80 nm Al_2O_3. AFM images and thickness profiles of $MoSe_2$ FETs are shown in Figure S7 in the Supporting Information. **Figure 3**a presents the schematic illustration of layered undoped $MoSe_2$ in which Mo atoms are sandwiched between Se atoms. Transfer characteristics show that undoped $MoSe_2$ is an n-type dominant semiconductor (Figure 3d). Its electronic mobility (μ) is calculated by the formula below

$$\mu = \frac{L}{W}\frac{1}{\varepsilon_0\varepsilon_r}\frac{d}{V_{ds}}\frac{dI_{ds}}{dV_{ds}} \quad (1)$$

where L and W are the channel length and width, respectively, d and ε_r are the thickness and relative dielectric constant of the Al_2O_3 layer, respectively, and ε_0 is the vacuum dielectric constant. For the undoped $MoSe_2$ FETs with 6.2 nm thickness, high mobility (13 $cm^2\ V^{-1}\ s^{-1}$) is achieved, which is larger than previous reports.[26,27] Simultaneously, the carrier concentration (n) of 5.25×10^{12} cm^{-2} can be acquired according to the formula below

$$n = \frac{1}{q}\frac{I_{ds}}{W}\frac{L}{V_{ds}}\frac{1}{\mu} \quad (2)$$

where q is the elemental charge. Compared with undoped $MoSe_2$, the 1% Ta-doped one shows lightly n-type dominant transfer characteristics (Figure S8, Supporting Information). 2% Ta-doped $MoSe_2$ shows ambipolar behavior (Figure 3b,e). The properties of 2% Ta-doped $MoSe_2$ are similar to that of intrinsic semiconductors, of which the charge neutrality point is ≈0 V. 3% Ta-doped $MoSe_2$ exhibits a p-type semiconductor (Figure 3c,f). For the 3% Ta-doped $MoSe_2$ FET with 6.2 nm thickness, the hole concentration and mobility of p-type $MoSe_2$ are 8.42×10^{11} cm^{-2} and 2.65 $cm^2\ V^{-1}\ s^{-1}$, respectively. Compared with electron mobility, the reduction of hole mobility may partly arise from the restrained transportation among valence bonds for holes but free transportation for electrons. Additionally, it may partly arise from larger contact resistance and charge scattering due to the doping.[28] However, it can be further improved via an optimized growth procedure.[29,30] Here, the undoped and Ta-doped $MoSe_2$ is successfully synthesized, which makes it possible to assemble electronic and optoelectronic devices.

2.2. Electronic and Optoelectronic Properties of $MoSe_2$ Homojunction Device

Homojunction devices play a significant role in fundamental electronics and are assembled by undoped and Ta-doped $MoSe_2$. **Figure 4**a,b exhibits the schematic and optical image of $MoSe_2$ homojunction diode based on undoped and Ta-doped $MoSe_2$. Undoped and 3% Ta-doped $MoSe_2$ flakes are mechanically exfoliated onto 80 nm Al_2O_3/Si substrate, respectively. Then the undoped $MoSe_2$ flake is transferred onto doped $MoSe_2$ flake via poly(vinyl alcohol) (PVA)-assisted dry transfer method. Cr/Au

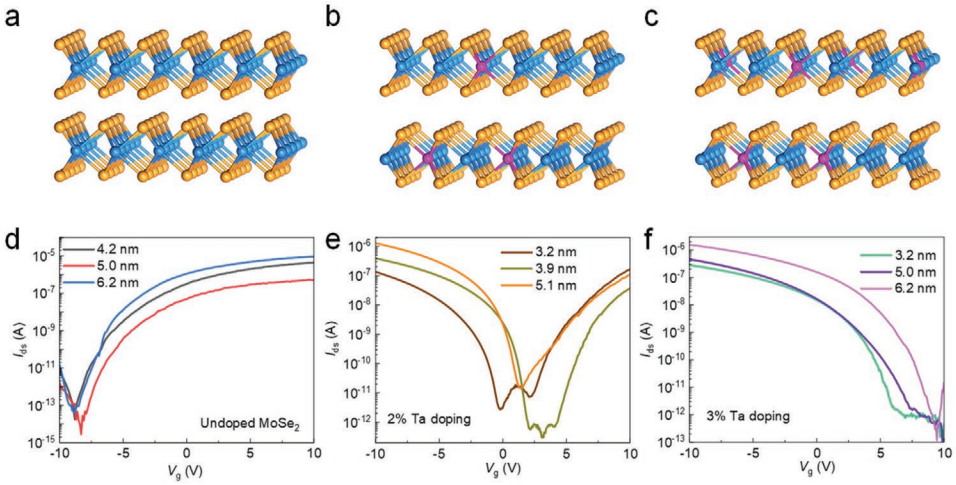

Figure 3. Atomic schematic views of $MoSe_2$ doped by Ta element and transfer characteristic curves of undoped and doped $MoSe_2$ FETs. a,d) Schematic illustration and transfer characteristic curves of $MoSe_2$ crystals without Ta element. b,e) Schematic illustration and transfer characteristic curves of $MoSe_2$ crystals with 2% Ta doping. c,f) Schematic illustration and transfer characteristic curves of $MoSe_2$ crystals with 3% Ta doping. All the transfer characteristics are obtained at 0.5 V bias voltage (V_{ds}).

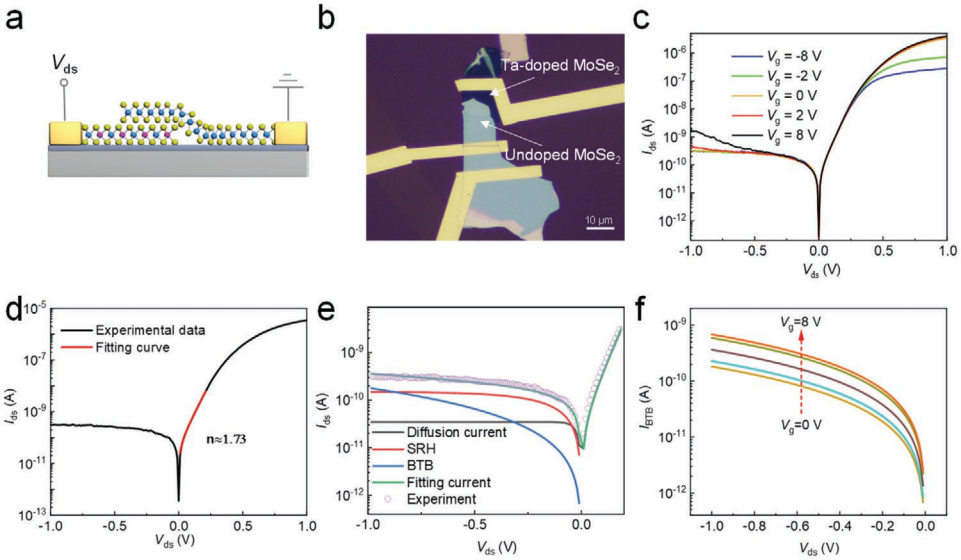

Figure 4. Electrical properties of $MoSe_2$ homojunction diode. a,b) Schematic illustration and optical microscopy image of $MoSe_2$ device, respectively. c) Output characteristics of $MoSe_2$ homojunction device under various gate voltages. d) I_{ds}–V_{ds} curve of $MoSe_2$ device at zero gate voltage. The red curve is the fitting result. e) Dark current components of $MoSe_2$ homojunction device at zero gate voltage. f) Band-to-band tunneling current (I_{BTB}) as a function of the bias voltage (V_{ds}) at gate voltage from 0 to 8 V with 2 V step.

electrodes are patterned and deposited via electron-beam lithography (EBL) and thermal evaporation, respectively. Then, a lift-off process is performed (detailed information in the Experimental Section). Ta-doped and undoped $MoSe_2$ serve as drain and source electrodes, respectively. Additionally, the cross-section of the homojunction is identified via high-resolution cross-sectional TEM (Figure S9, Supporting Information), which shows a clean interface. From the TEM image, the thickness of undoped and Ta-doped $MoSe_2$ is 23.7 and 5.5 nm, respectively. I_{ds}–V_{ds} curves of $MoSe_2$ homojunction diode are measured under various gate voltages (Figure 4c). The rectification ratio varies with the gate voltage and exceeds 10^4 at zero gate voltage. Besides, it possesses a low reverse current at zero gate voltage. Compared with other p–n junction devices, our homojunction photodetector is competent for the low power consumption device at zero gate voltage.[31,32] To evaluate the quality of the homojunction, we got the ideal factor (n) by fitting the output curve (black curve in Figure 4d) at $V_g = 0$ V, which follows the volt–ampere characteristic function below

$$I_{ds} = I_s\left(e^{\frac{qV_{ds}}{nkT}} - 1\right) \tag{3}$$

where I_s is reverse saturation current, q is elemental charge, $T = 300$ K is Kelvin temperature, and k is Boltzmann constant. The fitting result is shown in Figure 4d and $n \approx 1.73$ is acquired. For the diode, $n = 1$ indicates an ideal diode. For a factor larger than 1, a recombination current exists.[33] Analyzing dark current is crucial to the improvement of device performance. The dark current under various gate voltages was analyzed via the developed simultaneous data-processing technique.[34] Figure 4e shows the analysis results of dark current for $MoSe_2$ homojunction device at zero gate voltage. The fitting curve consists with that of the experimental result. The simulated ideal factor is ≈1.6 and near 1.73. At $V_{ds} > -0.88$ V, the Shockley–Read–Hall (SRH) current dominates, which possibly results from trap states in the gap.[35] Therefore, further improving the quality of the interface would decrease the SRH current. When V_{ds} is below −0.88 V, the band-to-band tunneling (BTB) current gradually increases and dominates. Because the large bias voltage makes the energy band bend steeply, which increases the tunneling probability. We also analyzed dark current at other gate voltages (Figure S10, Supporting Information). With gate voltage changing, the diffusion and SRH currents change scarcely. However, the BTB current becomes larger by increasing gate voltage from 0 to 8 V (Figure 4f). Because the band structure at the interface also becomes steeper for higher gate voltage, which results in a stronger built-in electric field and further enlarges the BTB probability.

Photovoltaic photodetectors are desired for high-performance photodetection and energy conversion. Here, an $MoSe_2$ homojunction photodetector is demonstrated, which operates at zero bias voltage and zero gate voltage. To demonstrate the response mechanism of the $MoSe_2$ photodetector clearly, an $MoSe_2$ photodetector is assembled to characterize photocurrent mapping (Figure S11, Supporting Information). Obviously, the photocurrent distributes in the junction region. It means that the photoresponse mainly results from the built-in electric field at the interface. **Figure 5**a shows the output characteristics of $MoSe_2$ photodetector under various power densities (P) illuminated by 830 nm wavelength. A photovoltaic response is obviously exhibited. Open-circuit voltage (V_{oc}) gradually reaches the saturation of 0.68 V (Figure 5b), which is higher than reported devices.[36,37] Short-circuit currents are also extracted and fitted by a power law

$$I_{sc} \propto P^{\alpha} \tag{4}$$

where α is a fitting parameter. The obtained $\alpha \approx 0.93$ indicates a good linear relationship. For photovoltaic detectors or solar cells, output electrical power ($P_{el} = I_{ds} \cdot V_{ds}$) is adopted to the

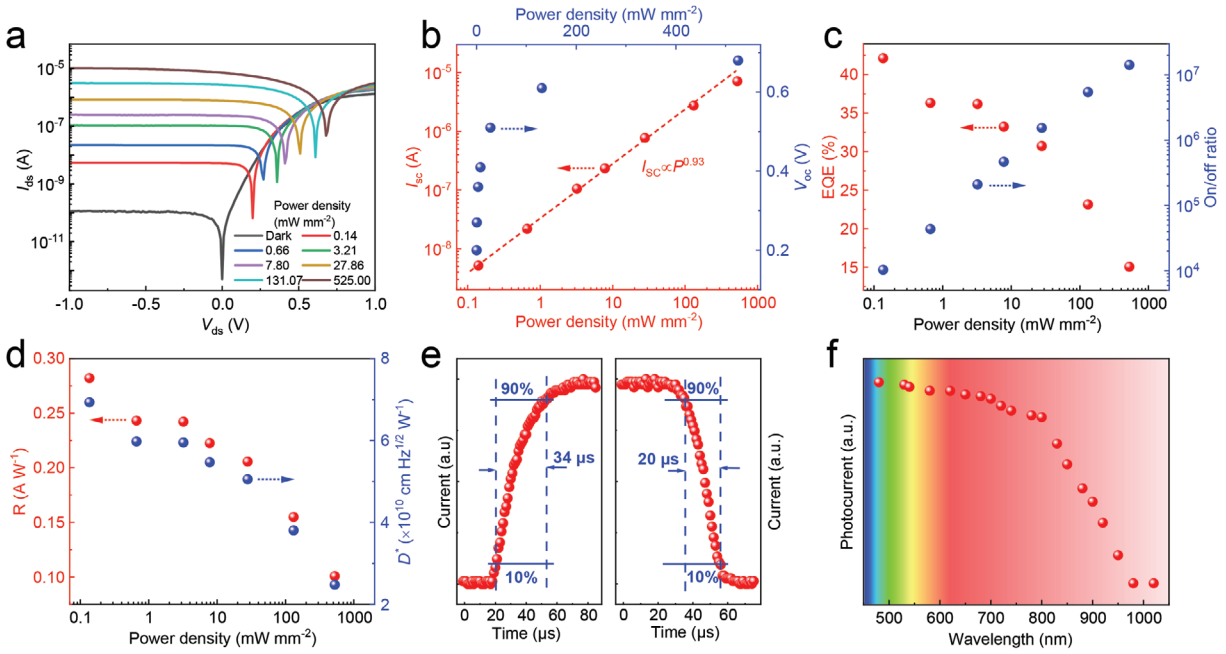

Figure 5. Photoresponse properties of $MoSe_2$ homojunction photodetector. a) Output characteristics of $MoSe_2$ homojunction photodetector under different power densities illuminated by 830 nm laser. b) Power-dependent open-circuit voltage (V_{oc}) and short-circuit current (I_{sc}). c) Power-dependent external quantum efficiency (EQE) and on/off ratio at a bias voltage of 0 V. d) Responsivity (R) and detectivity (D^*) as a function of power density illuminated by 830 nm. e) Time-resolved response of $MoSe_2$ homojunction photodetector at zero bias voltage. f) Photocurrent under various wavelengths.

electricity generation capability. For different power densities, the P_{el} and fill factor ($FF = P_{max}/I_{sc} \cdot V_{oc}$) are acquired in Figure S12a,b in the Supporting Information. The P_{el} increases with the increasing power density, while FF reaches the maximum of 0.66 and is followed by a decline. Concerning the homojunction photodetector, the maximum electrical power P_{max}, indicated by the shadow region (Figure S12c, Supporting Information), reaches up to 1.37 μW, which implies a potential in solar cells.[38] EQE, responsivity (R), and detectivity (D^*) are important parameters of photodetectors. The external quantum efficiency is defined by

$$EQE = \frac{hcI_{ph}}{q\lambda P_{in}} \tag{5}$$

where h is Planck's constant, c is the velocity of light, and λ is excitation wavelength. It is the ratio of the number of the photoinduced carrier to incident photons. The responsivity is calculated by

$$R = \frac{I_{ph}}{AP_{in}} \tag{6}$$

where I_{ph} is the photocurrent, A is active area, and P_{in} is optical power density. Detectivity is calculated by

$$D^* = R\sqrt{A}/\sqrt{\frac{4kT}{R_0}} \tag{7}$$

where R_0 is the resistance of the $MoSe_2$ homojunction device at zero bias. For the operation frequency larger than 300 Hz, the $1/f$ noise is negligible.[33] At zero bias voltage, the thermal noise dominates.[39] The EQE is calculated and shown in Figure 5c, which is as large as 42%. The high EQE benefits from a continuous energy band. Because carriers easily pass through the junction with no cusp or notch in conduction or valence bands. Figure 5c also shows the light on/off ratio, which increases for larger power density. $MoSe_2$ homojunction device exhibits ultrahigh light on/off ratio of ≈10^7, which means a high signal-to-noise ratio and is comparable to the reported work.[40] The excellent on/off ratio attributes to the ultralow dark current and high EQE. The responsivity and detectivity are extracted out and reach up to 0.28 A W^{-1} and 6.93×10^{10} cm $Hz^{1/2}$ W^{-1}, respectively, as shown in Figure 5d. To demonstrate response speed, $MoSe_2$ photodetectors are periodically illuminated under 830 nm laser with different power densities. The switching response is recorded and presented in Figure S12d in the Supporting Information. When the power density increases, the photocurrent simultaneously becomes larger. Notably, an obvious signal-to-noise ratio is observed. More importantly, the fast rise time (34 μs) and fall time (20 μs) are demonstrated (Figure 5e). One can find that $MoSe_2$-based homojunction photodetector possesses both high responsivity and fast response speed, which makes the $MoSe_2$ homojunction photodetector more competent to detect optical signals in time (**Table 1**). To further identify the detection wavelength of the $MoSe_2$ device, the photocurrent is plotted as the function of the wavelength from 480 to 1020 nm and shown in Figure 5f. The photocurrent decreases slowly in the visible region and rapidly in the near-infrared region (near 800 nm), which is coincident with the bandgap of $MoSe_2$. Besides, we also performed measurements of the $MoSe_2$ photodetector under 637 nm laser illumination.

Table 1. Parameters of reported TMDs photovoltaic photodetectors.

Materials	Doping method	Bias [V]	Wavelength [nm]	R [A W^{-1}]	EQE [%]	Time	Refs.
$MoSe_2/MoO_2$	Intrinsic property	3	532	0.1	23.5	1.2 s	[41]
$MoSe_2/WSe_2$	Intrinsic property	0	543	–	–	6 ms	[42]
Thin/thick-$MoSe_2$	Intrinsic property	0	635	1	–	10 ms	[43]
$WSe_2/MoSe_2$	Substitutional doping	0	638	0.33	–	1.5 ms	[44]
WSe_2/MoS_2	Intrinsic property	0	532	0.1	25	5 ms	[5]
MoS_2/WSe	Intrinsic property	0	532	0.12	34	–	[35]
p-$MoSe_2$/n-$MoSe_2$	Substitutional doping	0	405	≈0.2	40	–	[45]
p-MoS_2/n-MoS_2	Chemical doping	1	655	0.03	–	–	[46]
p-WSe_2/n-WSe_2	Laser-induced doping	0	633	≈0.8	–	136 µs	[47]
p-$MoSe_2$/n-$MoSe_2$	Substitutional doping	0	830	0.28	42	34 µs	This work

$MoSe_2$ photodetector also shows a high light on/off ratio (beyond 10^7) and fast response (99 µs) (Figure S13, Supporting Information). The measured electronic and photoelectronic properties show that the $MoSe_2$ homojunction photodetector possesses outstanding photoresponse.

2.3. $MoSe_2$ Inverter

Substitution doping also opens up huge possibilities in logic devices. To demonstrate the logic application, inverters are fabricated. **Figure 6**a shows the schematic of the $MoSe_2$ inverter, and the corresponding optical microscopy image and transfer characteristic curves are shown in Figure S14 in the Supporting Information. The thicknesses of the undoped and Ta-doped $MoSe_2$ flakes are 4.5 and 4.3 nm, respectively, identified via AFM (Figure S15, Supporting Information). Figure 6b exhibits the input voltage dependent on the output voltage of the $MoSe_2$ inverter at various supply voltages. The output voltage is equal to the supply voltage at low input voltage. It decreases to 0 V at high input voltage. Significantly, the output voltage drops rapidly from high level to low level. To quantitatively evaluate the inverter, the voltage gain is derived and defined as gain $= -dV_{out}/dV_{in}$. The gain is elevated gradually with increasing supply voltage and reaches up to 34 at $V_{ds} = 10$ V (Figure 6c). Such a high gain is higher than that of reported inverters (**Table 2**) and desired for logic circuits. It can be further improved by decreasing the thickness of the dielectric layer or adopting the dielectric materials with a high dielectric constant.[48,49] Figure 6d exhibits the power consumption under various supply voltages. The power consumption becomes larger with the supply voltage increasing and reaches up to ≈127 nW at $V_{ds} = 10$ V. Balancing the gain and power consumption, the $MoSe_2$ inverter is more suitable for the logic circuits with high gain and low power complementary.

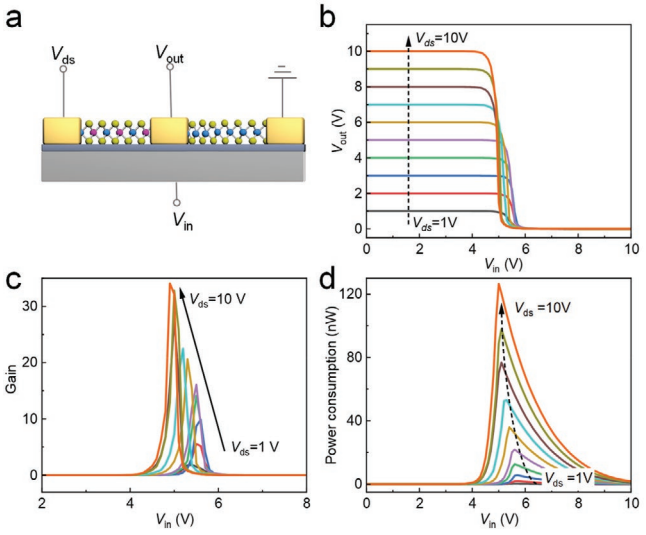

Figure 6. Electrical characteristics of MoS_2 inverter. a) Schematic illustration of the inverter, which is composed of p- and n-doped $MoSe_2$. Input port (V_{in}) and supply voltage (V_{ds}) connect the back gate and the Ta-doped $MoSe_2$, respectively. Output port (V_{out}) connects the undoped and doped $MoSe_2$ flakes. b) V_{out}–V_{in} curve under various voltages. c,d) Gain and power consumption of $MoSe_2$ inverter at various drain voltages.

3. Conclusion

In conclusion, the undoped and Ta-doped $MoSe_2$ crystals are successfully synthesized via substitutional doping, and conduction type is flexibly modulated from n-type behavior to ambipolar and p-type behaviors. The modulation of conductance type greatly extends the application of TMDCs. Based on the undoped and Ta-doped $MoSe_2$, high-performance homojunction photodetector and inverter are assembled. The homojunction photodetector shows an obvious photovoltaic response, stemming from the homojunction. It shows a large open-circuit voltage (0.68 V) and an output electrical power (1.37 µW), which indicates the potential in microcell applications. Importantly, the photodetector exhibits a large responsivity (0.28 A W^{-1}) and external quantum efficiency (42%). Moreover, fast rise time (34 µs) and fall time (20 µs) are demonstrated. Excellent and fast photoresponse exhibits the advantage of homojunction. Besides, the $MoSe_2$ inverter exhibits a high gain of 34 and low power consumption of 127 nW. Such a large gain is desired for excellent logic circuits. Our works lay the foundation of substitutional doping in 2D materials and provide an opportunity to fabricate excellent electronics and optoelectronics based on 2D materials.

Table 2. Comparison of reported TMDC inverters.

Materials	Doping method	Bias voltage [V]	Gain	Power consumption [nW]	Refs.
WSe_2/IGZO	Intrinsic property	5	14	–	[50]
p-WSe_2/n-WSe_2	Chemical doping	9	10	≈0.17	[51]
p-$MoSe_2$/n-$MoSe_2$	Substitutional doping	1	0.5	–	[45]
WSe_2/$MoSe_2$	Intrinsic property	3	23	–	[52]
MoS_2/WSe_2	Intrinsic property	2	11.6	≈0.07	[53]
p-$MoTe_2$/n-$MoTe_2$	Laser-induced doping	2	28	120	[54]
p-$MoSe_2$/n-$MoSe_2$	Substitutional doping	10	34	127	This work

4. Experimental Section

Material Synthesis: Both the undoped and Ta-doped $MoSe_2$ crystals were prepared via CVT. For undoped $MoSe_2$ crystals, Mo power (99.999%) and Se powder (99.999%) were mixed fully with the molar ratio of 1:6. The mixture was sealed in a quartz tube at 10^{-6} mbar. Iodine power was also sealed into the same tube and served as a transport agent. The tube was placed in a two-zone furnace. The source and growth zones were set to 780 and 980 °C, gradually. Both zones were kept for 9000 min. Finally, the undoped $MoSe_2$ crystals were synthesized. For Ta-doped $MoSe_2$ crystals, the Ta power (99.999%, molar ratio of 1%, 2%, and 3% for doping, respectively) was added into the mixture (mentioned above). The iodine power served as the transport agent. The mixture was sealed in a quartz tube at 10^{-6} mbar and placed in a two-zone furnace. The source and growth zones were set to 790 and 1050 °C, respectively, for 9000 min. After the process, the two-zone furnace was slowly cooled to room temperature and Ta-doped $MoSe_2$ crystals were synthesized.

Material Characterization: The atomically resolved ADF-STEM was performed using a Nion HERMES 200 microscope. Transmission electron microscope (JEOL JEM-2100F) was performed for TEM images and EDS element mappings. XRD was conducted by Bruker D8 X-ray diffractometer. Raman spectra were measured by HR800 with 532 nm laser. The thickness profiles were acquired by AFM (Bruker MultiMode 8).

Simulation: For band simulation, first-principles calculations were performed with Vienna Ab-initio Simulation Package (VASP), and the projector augmented wave (PAW) method was adopted.[55–57] The exchange–correlation interactions were addressed with Perdew–Burke–Ernzerhof (PBE) functional.[58] Plane-wave cutoff energy was set to 500 eV. Lattice constants and atom coordinates were relaxed via the conjugate gradient method with energy and force convergence criteria of 10^{-9} eV and 10^{-4} eV Å^{-1}, respectively. For the first Brillouin zone sampling, Γ-centered Monkhorst–Pack *k*-point meshes of $11 \times 11 \times 9$ and $11 \times 11 \times 1$ were used to sample the unit cell of bulk and monolayer during structure relaxation. The optB88-vdW scheme was employed to take van der Waals interactions into account.[59] In addition, a 15 Å vacuum spacing was added to reduce the artificial interactions between adjacent monolayers. To investigate the effect of Ta dopant, $3 \times 3 \times 2$ and $4 \times 4 \times 1$ supercells of bulk and monolayer $MoSe_2$ were respectively constructed. For the current analysis, dark current characteristics were analyzed by the series of separated current component models, including minority carrier diffusion current, band-to-band tunneling current, and generation-recombination current.[60,61] By fitting the dark current of device under zero and small forward bias, the reverse saturation current and ideal factor can be obtained. Trap-assisted recombination (dominated by SRH process for the uncontrollable defects) was dominated under middle reverse bias. The band-to-band tunneling process always happens when the electric field in the junction is large enough. The SRH current and band-to-band current in the analytical model is fitted by $ae^{bV^{-1}}$ and $mVe^{nV^{-1}}$, respectively, where *a*, *b*, *m*, and *n* are the fitted parameters.

Device Fabrication and Measurement: Undoped and doped $MoSe_2$ flakes were mechanically exfoliated onto 80 nm Al_2O_3/Si substrates using Scotch tape, respectively. Then, a PVA film was attached onto the exfoliated undoped $MoSe_2$ flake. The PVA/undoped $MoSe_2$ flake was transferred onto the Ta-doped $MoSe_2$ flake using a homemade transfer system. After the dissolution of PVA film in deionized water, the homojunction photodetector was fabricated. For the inverter device, the undoped $MoSe_2$ was transferred near the Ta-doped one with the method mentioned above. Electron-beam lithography (FEI F50) was used to define the source and drain patterns. The thermal evaporation and the lift-off process were conducted to fabricate the electrodes (15 nm Cr/45 nm Au). All the $MoSe_2$ FET, photodetector, and inverter were measured in the atmosphere and at room temperature. The Agilent B1500 semiconductor parameter analyzer was utilized to analyze the electronic and photoelectronic properties of $MoSe_2$ devices, which were put in the lakeshore probe station. The time-resolved speed was recorded by Tektronix Oscilloscope MDO3014. For response spectra, a light source (YSL, SC-PRO) was modulated by Omni monochromator, and response curves were recorded by a source meter (Keithley, B2192A). The photocurrent mapping was measured by a homemade photocurrent scanning system.

Supporting Information

Supporting Information is available from the Wiley Online Library or from the author.

Acknowledgements

This work was supported by the National Natural Science Foundation of China (Grant Nos. 31900748, 61975224, and 61904184), the Fund of Shanghai Natural Science Foundation (Grant Nos. 19XD1404100, 18ZR1445800, and 21YF1454900), the Key Research Program of the Chinese Academy of Sciences (Grant No. XDPB22), the Special Grants and Science Foundation from China Post-doctoral Science Foundation (Grant Nos. 2019TQ0334, 2020M671246, and BX2021330), the Innovation Project of Shanghai Institute of Technical Physics (Grant No. CX-352), and the Youth Innovation Promotion Association CAS. The authors acknowledge the Electron Microscopy Laboratory of Peking University for the use of electron microscopes.

Conflict of Interest

The authors declare no conflict of interest.

Author Contributions

F.Z. and J.Y. contributed equally to this work. W.H., Z.W., L.Z., and Z.F. conceived the project. F.Z., T.X., Y.W., H.W., T.H., and Y.Y. fabricated the devices. F.Z. and Z.Z. performed electronic and photoelectronic

characterizations. J.Y. and Z.W. synthesized the $MoSe_2$ crystals. J.G. conducted the XRD characterizations. B.H. conducted the STEM characterizations under the direction of P.G. X.G. performed the DFT calculations under the direction of X.Z. Q.L. performed the current simulations. J.Y. conducted the AFM experiments. M.P. performed the speed measurements. P.W. performed the spectra experiments. P.W., T.H., and M.Z. assisted in analyzing experiments. All authors discussed the results and revised the manuscript.

Data Availability Statement

Research data are not shared.

Keywords

inverters, $MoSe_2$, photodetectors, substitutional doping

Received: May 17, 2021
Revised: August 11, 2021
Published online: October 13, 2021

[1] L. Li, W. Wang, P. Gong, X. Zhu, B. Deng, X. Shi, G. Gao, H. Li, T. Zhai, *Adv. Mater.* **2018**, *30*, 1706771.
[2] S.-Y. Kim, J. Kwak, C. V. Ciobanu, S.-Y. Kwon, *Adv. Mater.* **2019**, *31*, 1804939.
[3] Y. Chen, Y. Wang, Z. Wang, Y. Gu, Y. Ye, X. Chai, J. Ye, Y. Chen, R. Xie, Y. Zhou, Z. Hu, Q. Li, L. Zhang, F. Wang, P. Wang, J. Miao, J. Wang, X. Chen, W. Lu, P. Zhou, W. Hu, *Nat. Electron.* **2021**, *4*, 357.
[4] K. Zhang, X. Fang, Y. Wang, Y. Wan, Q. Song, W. Zhai, Y. Li, G. Ran, Y. Ye, L. Dai, *ACS Appl. Mater. Interfaces* **2017**, *9*, 5392.
[5] W. Deng, C. You, X. Chen, Y. Wang, Y. Li, B. Feng, K. Shi, Y. Chen, L. Sun, Y. Zhang, *Small* **2019**, *15*, 1901544.
[6] H. W. Liu, X. L. Zhu, X. X. Sun, C. G. Zhu, W. Huang, X. H. Zhang, B. Y. Zheng, Z. X. Zou, Z. Y. Luo, X. Wang, D. Li, A. L. Pan, *ACS Nano* **2019**, *13*, 13573.
[7] X. Zhang, L. Huangfu, Z. Gu, S. Xiao, J. Zhou, H. Nan, X. Gu, K. Ostrikov, *Small* **2021**, *17*, 2007312.
[8] G. Gao, B. Wan, X. Liu, Q. Sun, X. Yang, L. Wang, C. Pan, Z. L. Wang, *Adv. Mater.* **2018**, *30*, 1705088.
[9] Y. J. Park, A. K. Katiyar, A. T. Hoang, J.-H. Ahn, *Small* **2019**, *15*, 1901772.
[10] S. W. LaGasse, P. Dhakras, K. Watanabe, T. Taniguchi, J. U. Lee, *Adv. Mater.* **2019**, *31*, 1901392.
[11] L. Lv, F. Zhuge, F. Xie, X. Xiong, Q. Zhang, N. Zhang, Y. Huang, T. Zhai, *Nat. Commun.* **2019**, *10*, 3331.
[12] J. Sun, Y. Wang, S. Guo, B. Wan, L. Dong, Y. Gu, C. Song, C. Pan, Q. Zhang, L. Gu, F. Pan, J. Zhang, *Adv. Mater.* **2020**, *32*, 1906499.
[13] K. Dolui, I. Rungger, C. Das Pemmaraju, S. Sanvito, *Phys. Rev. B* **2013**, *88*, 075420.
[14] J. Suh, T.-E. Park, D.-Y. Lin, D. Fu, J. Park, H. J. Jung, Y. Chen, C. Ko, C. Jang, Y. Sun, R. Sinclair, J. Chang, S. Tongay, J. Wu, *Nano Lett.* **2014**, *14*, 6976.
[15] T. Momose, A. Nakamura, M. Daniel, M. Shimomura, *AIP Adv.* **2018**, *8*, 025009.
[16] J.-K. Qin, W.-Z. Shao, C.-Y. Xu, Y. Li, D.-D. Ren, X.-G. Song, L. Zhen, *ACS Appl. Mater. Interfaces* **2017**, *9*, 15583.
[17] J. Liu, X. Liu, Z. Chen, L. Miao, X. Liu, B. Li, L. Tang, K. Chen, Y. Liu, J. Li, Z. Wei, X. Duan, *Nano Res.* **2019**, *12*, 463.
[18] Y. Fu, M. Long, A. Gao, Y. Wang, C. Pan, X. Liu, J. Zeng, K. Xu, L. Zhang, E. Liu, W. Hu, X. Wang, F. Miao, *Appl. Phys. Lett.* **2017**, *111*, 043502.
[19] S.-S. Chee, H. Jang, K. Lee, M.-H. Ham, *ACS Appl. Mater. Interfaces* **2020**, *12*, 31804.
[20] M. Bougouma, B. Guel, T. Segato, J. B. Legma, M.-P. D. Ogletree, *Bull. Chem. Soc. Ethiop.* **2008**, *22*, 225.
[21] W. Zhou, X. Zou, S. Najmaei, Z. Liu, Y. Shi, J. Kong, J. Lou, P. M. Ajayan, B. I. Yakobson, J.-C. Idrobo, *Nano Lett.* **2013**, *13*, 2615.
[22] J. Lin, S. T. Pantelides, W. Zhou, *ACS Nano* **2015**, *9*, 5189.
[23] X. Wang, Y. Gong, G. Shi, W. L. Chow, K. Keyshar, G. Ye, R. Vajtai, J. Lou, Z. Liu, E. Ringe, B. K. Tay, P. M. Ajayan, *ACS Nano* **2014**, *8*, 5125.
[24] P. Tonndorf, R. Schmidt, P. Böttger, X. Zhang, J. Börner, A. Liebig, M. Albrecht, C. Kloc, O. Gordan, D. R. T. Zahn, S. Michaelis de Vasconcellos, R. Bratschitsch, *Opt. Express* **2013**, *21*, 4908.
[25] X. Zheng, Y. Wei, J. Liu, S. Wang, J. Shi, H. Yang, G. Peng, C. Deng, W. Luo, Y. Zhao, Y. Li, K. Sun, W. Wan, H. Xie, Y. Gao, X. Zhang, H. Huang, *Nanoscale* **2019**, *11*, 13469.
[26] D. Somvanshi, E. Ber, C. S. Bailey, E. Pop, E. Yalon, *ACS Appl. Mater. Interfaces* **2020**, *12*, 36355.
[27] W. T. Kang, T. L. Phan, K. J. Ahn, I. Lee, Y. R. Kim, U. Y. Won, J. E. Kim, Y. H. Lee, W. J. Yu, *ACS Appl. Mater. Interfaces* **2021**, *13*, 18056.
[28] X. Duan, C. Wang, Z. Fan, G. Hao, L. Kou, U. Halim, H. Li, X. Wu, Y. Wang, J. Jiang, A. Pan, Y. Huang, R. Yu, X. Duan, *Nano Lett.* **2016**, *16*, 264.
[29] S. K. Pandey, H. Alsalman, J. G. Azadani, N. Izquierdo, T. Low, S. A. Campbell, *Nanoscale* **2018**, *10*, 21374.
[30] F. Zhang, Y. Lu, D. S. Schulman, T. Zhang, K. Fujisawa, Z. Lin, Y. Lei, A. L. Elias, S. Das, S. B. Sinnott, M. Terrones, *Sci. Adv.* **2019**, *5*, eaav5003.
[31] S. W. Cao, Y. H. Xing, J. Han, X. Luo, W. X. Lv, W. M. Lv, B. S. Zhang, Z. M. Zeng, *Nanoscale* **2018**, *10*, 16805.
[32] A. Varghese, D. Saha, K. Thakar, V. Jindal, S. Ghosh, N. V. Medhekar, S. Ghosh, S. Lodha, *Nano Lett.* **2020**, *20*, 1707.
[33] Y. Tang, Z. Wang, P. Wang, F. Wu, Y. Wang, Y. Chen, H. Wang, M. Peng, C. Shan, Z. Zhu, S. Qin, W. Hu, *Small* **2019**, *15*, 1805545.
[34] W. D. Hu, X. S. Chen, Z. H. Ye, W. Lu, *Appl. Phys. Lett.* **2011**, *99*, 091101.
[35] C.-H. Lee, G.-H. Lee, A. M. van der Zande, W. Chen, Y. Li, M. Han, X. Cui, G. Arefe, C. Nuckolls, T. F. Heinz, J. Guo, J. Hone, P. Kim, *Nat. Nanotechnol.* **2014**, *9*, 676.
[36] W. Wu, Q. Zhang, X. Zhou, L. Li, J. Su, F. Wang, T. Zhai, *Nano Energy* **2018**, *51*, 45.
[37] C. Tan, H. Wang, X. Zhu, W. Gao, H. Li, J. Chen, G. Li, L. Chen, J. Xu, X. Hu, L. Li, T. Zhai, *ACS Appl. Mater. Interfaces* **2020**, *12*, 44934.
[38] F. Wu, Q. Li, P. Wang, H. Xia, Z. Wang, Y. Wang, M. Luo, L. Chen, F. Chen, J. Miao, X. Chen, W. Lu, C. Shan, A. Pan, X. Wu, W. Ren, D. Jariwala, W. Hu, *Nat. Commun.* **2019**, *10*, 4663.
[39] M. Peng, R. Xie, Z. Wang, P. Wang, F. Wang, H. Ge, Y. Wang, F. Zhong, P. Wu, J. Ye, Q. Li, L. Zhang, X. Ge, Y. Ye, Y. Lei, W. Jiang, Z. Hu, F. Wu, X. Zhou, J. Miao, J. Wang, H. Yan, C. Shan, J. Dai, C. Chen, X. Chen, W. Lu, W. Hu, *Sci. Adv.* **2021**, *7*, eabf7358.
[40] F. Wu, H. Xia, H. D. Sun, J. W. Zhang, F. Gong, Z. Wang, L. Chen, P. Wang, M. S. Long, X. Wu, J. L. Wang, W. C. Ren, X. S. Chen, W. Lu, W. D. Hu, *Adv. Funct. Mater.* **2019**, *29*, 1900314.
[41] N. Wazir, R. Liu, C. Ding, X. Wang, X. Ye, X. Lingling, T. Lu, L. Wei, B. Zou, *ACS Appl. Nano Mater.* **2020**, *3*, 7543.
[42] S. Jia, Z. Jin, J. Zhang, J. Yuan, W. Chen, W. Feng, P. Hu, P. M. Ajayan, J. Lou, *Small* **2020**, *16*, 2002263.
[43] Y. Yang, N. Huo, J. Li, *J. Mater. Chem. C* **2017**, *5*, 7051.
[44] J. E. Kim, W. T. Kang, V. T. Vu, Y. R. Kim, Y. S. Shin, I. Lee, U. Y. Won, B. H. Lee, K. Kim, T. L. Phan, Y. H. Lee, W. J. Yu, *J. Mater. Chem. C* **2021**, *9*, 3504.
[45] Y. Jin, D. H. Keum, S.-J. An, J. Kim, H. S. Lee, Y. H. Lee, *Adv. Mater.* **2015**, *27*, 5534.

[46] H.-M. Li, D. Lee, D. Qu, X. Liu, J. Ryu, A. Seabaugh, W. J. Yoo, *Nat. Commun.* **2015**, *6*, 6564.
[47] J. Chen, Q. Wang, Y. Sheng, G. Cao, P. Yang, Y. Shan, F. Liao, Z. Muhammad, W. Bao, L. Hu, R. Liu, C. Cong, Z.-J. Qiu, *ACS Appl. Mater. Interfaces* **2019**, *11*, 43330.
[48] G. Kim, H. S. Shin, *Nanoscale* **2020**, *12*, 5286.
[49] L. Wu, J. Shi, Z. Zhou, J. Yan, A. Wang, C. Bian, J. Ma, R. Ma, H. Liu, J. Chen, Y. Huang, W. Zhou, L. Bao, M. Ouyang, S. T. Pantelides, H.-J. Gao, *Nano Res.* **2020**, *13*, 1127.
[50] S. Lee, H. S. Lee, S. Yu, J. H. Park, H. Bae, S. Im, *Adv. Electron. Mater.* **2020**, *6*, 2000026.
[51] H. G. Ji, P. Solís-Fernández, D. Yoshimura, M. Maruyama, T. Endo, Y. Miyata, S. Okada, H. Ago, *Adv. Mater.* **2019**, *31*, 1903613.
[52] M.-H. Chiu, H.-L. Tang, C.-C. Tseng, Y. Han, A. Aljarb, J.-K. Huang, Y. Wan, J.-H. Fu, X. Zhang, W.-H. Chang, D. A. Muller, T. Takenobu, V. Tung, L.-J. Li, *Adv. Mater.* **2019**, *31*, 1900861.
[53] J. Wang, X. Guo, Z. Yu, Z. Ma, Y. Liu, Z. Lin, M. Chan, Y. Zhu, X. Wang, Y. Chai, *Adv. Funct. Mater.* **2020**, *30*, 2003859.
[54] J. Chen, J. Zhu, Q. Wang, J. Wan, R. Liu, *Small* **2020**, *16*, 2001428.
[55] G. Kresse, J. Furthmüller, *Phys. Rev. B* **1996**, *54*, 11169.
[56] G. Kresse, J. Furthmüller, *Comput. Mater. Sci.* **1996**, *6*, 15.
[57] P. E. Blöchl, *Phys. Rev. B* **1994**, *50*, 17953.
[58] J. P. Perdew, K. Burke, M. Ernzerhof, *Phys. Rev. Lett.* **1996**, *77*, 3865.
[59] J. Klimeš, D. R. Bowler, A. Michaelides, *J. Phys.: Condens. Matter* **2009**, *22*, 022201.
[60] V. Gopal, S. K. Singh, R. M. Mehra, *Infrared Phys. Technol.* **2002**, *43*, 317.
[61] W. D. Hu, X. S. Chen, F. Yin, Z. J. Quan, Z. H. Ye, X. N. Hu, Z. F. Li, W. Lu, *J. Appl. Phys.* **2009**, *105*, 104502.